



Photoreforming of ethylene glycol over Rh/TiO₂ and Rh/GaN:ZnO



Tobias F. Berto^a, Kai E. Sanwald^a, Wolfgang Eisenreich^a, Oliver Y. Gutiérrez^{a,*}, Johannes A. Lercher^{a,b,*}

^aTU München, Department of Chemistry and Catalysis Research Center, Lichtenbergstrasse 4, D-85747 Garching, Germany

^bPacific Northwest National Laboratory, Institute for Integrated Catalysis and Environmental Molecular Sciences Laboratory, P.O. Box 999, Richland, WA, USA

ARTICLE INFO

Article history:

Received 5 January 2016

Revised 16 February 2016

Accepted 17 February 2016

Keywords:

Photocatalysis

Photoreforming

H₂ production

Oxidation mechanisms

ABSTRACT

Photoreforming of diols, such as ethylene glycol, proceeds through a sequence of anodic oxidations, which enable the parallel formation of H₂ by reduction of H⁺ at the cathode. The anodic oxidation of ethylene glycol on Rh/TiO₂ leads to glycolaldehyde, formaldehyde and acetaldehyde as primary products. Glycolaldehyde is further converted *via* oxidative C–C-cleavage to formaldehyde and formic acid. Formaldehyde is oxidized to formic acid forming CO₂ and H₂. Acetaldehyde is oxidized to acetic acid, which decarboxylates to CO₂ and CH₄. Two catalytically active sites are proposed. On terminal Ti^{IV}–OH groups, oxygenates are oxidized *via* direct hole transfer to alkoxy-radicals prior to β–C–bond cleavage. Bridged [Ti–O–Ti]⁺ sites, in contrast, cleave a C–H bond, forming carbon centered radicals, which are further oxidized by transferring an electron to the conduction band of the semiconductor. On Rh/GaN:ZnO, glycolaldehyde is the main product, forming higher oxidized C2-oxygenates in turn by reaction with free oxygen radicals formed as product of OH[−] photocatalytic oxidation. The overall rates of photoreforming and, hence, H₂ evolution, depend mainly on the surface concentration of the compounds which are oxidized, while the nature of the oxygenate is of less importance.

© 2016 Elsevier Inc. All rights reserved.

1. Introduction

Photocatalytic reforming of polyols and sugars has been discussed as a promising route to carbon-neutral H₂ [1,2]. The technology may provide simpler pathways compared to overall water splitting, as the recombination of H₂ and O₂ is avoided [3] and separation is greatly facilitated. The wide abundance of oxygenate contaminants in water would make this even a preferred route, coupling water cleaning with storing photon energy in H₂. Methanol and polyols can be quantitatively photoreformed to CO₂–H₂ mixtures, [4–6] while the overall H₂ evolution rates have been reported to depend on the nature of the oxygenate [7,8]. Little agreement exists, however, on the evolution of intermediates and side-products, as well as the kinetics of the associated overall processes and elementary steps [6,7,9–11].

In photoreforming of glycerol, the first oxidation step is proposed to be initiated by ·OH-radicals or holes [6,9,11]. As expected from the Fenton's reagent chemistry, alcohols are oxidized to aldehydes [6] or carboxylic acids [9,11]. Subsequent C–C-cleavage is attributed to decarboxylation [9,11] or decarbonylation, using

water–gas shift to rationalize the observation of CO₂ [6]. The anodic half reactions during photooxidation of polyols on TiO₂ proceed *via* a different route [12]. Terminal OH-groups and surface lattice oxygen [Ti–O–Ti] sites facilitate direct and indirect hole transfer, respectively. In both cases, the carbon radicals are oxidized by reacting with molecular oxygen. The formation of CO has been attributed to the dehydration of formic acid formed intermediately during methanol reforming [13–16]. The pathway to CO formation in reforming of higher oxygenates is unclear. The ambiguity in the reaction path analyses and the contradiction in the existing hypotheses require to probe photoreforming under well-defined conditions and to identify the nature and kinetics of transformations of reactants, intermediates, and products of photocatalytic reforming.

The reaction is catalyzed, in principle, by a variety of semiconductors in the presence of UV- or visible light, including TiO₂ or alkaline earth titanates with metal co-catalysts, [1,2] as well as oxynitrides (e.g., TaON, LaTaON₂, Y₂Ta₂O₅N₂, and GaN:ZnO) [1,2,17]. Therefore, the chemistry on two typical representatives, i.e., AEROXIDE® TiO₂ P 25 (in this manuscript abbreviated as TiO₂) and GaN:ZnO as semiconductors is explored using Rh as co-catalyst. It should be noted in passing that the less positive valence band edge potential of the visible-light absorbing semiconductors, e.g., GaN:ZnO (band gap: 2.7 eV), leads to a lower oxidation potential compared to UV-light absorbing semiconductors,

* Corresponding authors at: TU München, Department of Chemistry and Catalysis Research Center, Lichtenbergstrasse 4, D-85747 Garching, Germany (J.A. Lercher). Fax: +49 (0) 89 289 13544.

E-mail addresses: oliver.gutierrez@mytum.de (O.Y. Gutiérrez), johannes.lercher@ch.tum.de (J.A. Lercher).

e.g., TiO_2 (band gap: 3.1 eV) [18,19]. The present contribution aims, therefore, to describe on a molecular level the elementary reactions involved in photoreforming using ethylene glycol (EG) as model reactant [20,21]. The simplicity of EG allows unambiguous identification of the involved elementary steps. The reaction pathway analysis and kinetics are based on quantitative gas and liquid phase analysis linked in a kinetic model [22–24].

2. Experimental section

2.1. Materials

All chemicals were obtained from commercial suppliers and used as provided: AEROXIDE® TiO_2 P 25 (Evonik, LOT: 4162092398), sodium hexachlororhodate (III) (Alfa Aesar, Rh 17.1%), gallium oxide (ABCR, 99.99%, LOT: 1040437), zinc oxide (ABCR, 99.7%, LOT: 1121535), ammonia (NH_3 , BASF, 5.0, anhydrous), synthetic air (Westfalen), hydrogen (H_2 , Westfalen, 5.0), argon (Ar, Westfalen, 5.0), nitrogen (N_2 , Westfalen, 5.0), ethanol (80 mg/100 mL, European Reference Materials), glyoxal trimer dihydrate (Fluka, $\geq 95\%$), EG (VWR-Chemicals, 99.9%), glycolaldehyde dimer (Aldrich), glycolic acid (Aldrich, 99%), glyoxylic acid monohydrate (Aldrich, 98%), formaldehyde solution (Fluka, 1000 $\mu\text{g mL}^{-1}$ in H_2O , IC Standard), formic acid (Merck, 98–100%), methanol (Aldrich, 99.8%, anhydrous), phloroglucinol (Aldrich, $\geq 99\%$), acetaldehyde solution (Aldrich, 35 wt.%), D_2O (Euriso-Top, 98.85 atom%), deuterium chloride in D_2O (Acros Organics, 1 M, 99.8 atom%), gallium ICP-standard (Merck, Certipur, 1000 mg L^{-1}), zinc ICP-standard (Merck, Certipur, 1000 mg L^{-1}), Rh AAS-standard (Fluka, TraceCert, $999 \pm 9 \text{ mg L}^{-1}$), Rh-foil (was provided by ESRF/BM25 station), and rhodium(III)oxide (Fluka, anhydrous, puriss).

2.2. Catalyst preparation

Synthesis of 1.0 wt.% $\text{RhO}_x/\text{TiO}_2$. TiO_2 was dried under static air at 473 K for 2 h prior to impregnation. The support (BET surface area: 53 $\text{m}^2 \text{g}^{-1}$ and pore volume of 0.11 mL g^{-1}) was treated with an aqueous solution of $\text{Na}_3\text{RhCl}_6 \cdot 12\text{H}_2\text{O}$ via incipient wetness impregnation. The reddish powder was kept at 383 K (5 K min^{-1}) for 1 h, and heat treated in synthetic air at 623 K (5 K min^{-1}) for 1 h (100 mL min^{-1}). After cooling to room temperature, the $\text{RhO}_x/\text{TiO}_2$ material was treated by heating with an increment of 5 K min^{-1} to 623 K in H_2 (100 mL min^{-1}) and cooled to room temperature. Subsequently, the sample was washed thoroughly to remove NaCl and dried in N_2 at 383 K overnight. Within the study used, parent TiO_2 was subjected to identical treatments such as $\text{RhO}_x/\text{TiO}_2$. 1.0 wt.% Pt/TiO_2 was synthesized using H_2PtCl_6 as Pt precursor, following the synthesis procedure used to prepare $\text{RhO}_x/\text{TiO}_2$.

Synthesis of 1.0 wt.% $\text{RhO}_x/(\text{Ga}_{1-x}\text{Zn}_x)(\text{N}_{1-x}\text{O}_x)$. $\text{RhO}_x/(\text{Ga}_{1-x}\text{Zn}_x)(\text{N}_{1-x}\text{O}_x)$ was synthesized according to a procedure reported by Domen et al. [19]. A physical mixture of 0.6 g (3.2 mmol) Ga_2O_3 and 0.520 g (6.4 mmol) ZnO was treated at 1098 K (10 K min^{-1}) for 16 h under NH_3 flow (200 mL min^{-1}). The obtained solid solution was cooled to room temperature under NH_3 flow and was subsequently treated at 873 K (5 K min^{-1}) for 1 h under synthetic airflow (50 mL min^{-1}). This procedure is defined as post-calcination in agreement with Ref. [19]. Post-calcined $(\text{Ga}_{1-x}\text{Zn}_x)(\text{N}_{1-x}\text{O}_x)$ ($x = 0.14$) was modified with RhO_x (denoted as a co-catalyst) by wet impregnation. In an evaporating dish 0.2 g of $(\text{Ga}_{1-x}\text{Zn}_x)(\text{N}_{1-x}\text{O}_x)$ was dispersed in 1 mL of bidistilled water ($\sigma = 18.2 \text{ M}\Omega \text{ cm}$) containing the appropriate amount of $\text{Na}_3\text{RhCl}_6 \cdot 12\text{H}_2\text{O}$. The stirred suspension was evaporated to dryness. The obtained powder was kept in static air at 623 K (5 K min^{-1}) for

1 h in order to obtain the RhO_x -decorated $(\text{Ga}_{1-x}\text{Zn}_x)(\text{N}_{1-x}\text{O}_x)$ solid solution. After cooling to room temperature the sample was washed to remove NaCl and dried in N_2 at 383 K overnight.

Different procedures of co-catalyst preparation were chosen in order to obtain photocatalysts with a maximum activity. $\text{Rh}/(\text{Ga}_{1-x}\text{Zn}_x)(\text{N}_{1-x}\text{O}_x)$, which was obtained by reducing RhO_x -decorated $(\text{Ga}_{1-x}\text{Zn}_x)(\text{N}_{1-x}\text{O}_x)$ in H_2 flow, possessed poor photocatalytic activity. We hypothesize that H_2 partially reduced Zn^{2+} -centers to create oxygen vacancies and, thus, increased the electron-hole recombination rate. In contrast, the best $\text{RhO}_x/\text{TiO}_2$ was obtained by treatment in synthetic air at 623 K (5 K min^{-1}) for 1 h and in H_2 at 623 K (5 K min^{-1}) for 1 h. H_2 treatment at 623 K may create oxygen vacancies on TiO_2 [25,26] and thus decrease electron hole recombination rates increasing photocatalytic performance [27]. As the reaction pathways and its selectivities were not significantly altered by this treatment, this phenomenon was not further studied.

2.3. Photocatalytic test

Photoreforming experiments. Photocatalytic reactions were carried out in a photo-reactor connected to a gas-tight gas circulation system (leakage rate $< 5 \cdot 10^{-4} \text{ Pa s}^{-1} \text{ L}^{-1}$, $V = 310 \text{ mL}$), the catalyst being exposed to light via top-irradiation through a quartz-window. 75 mg of photocatalyst was suspended in 100 mL of an aqueous solution containing the reactant (typically 20 mM). The reactor was kept at 288 K and the system was filled with Ar to 1 bar. The system was evacuated four times in order to remove O_2 . Completeness of O_2 removal was verified by GC analysis ($< 0.3 \mu\text{mol O}_2/\text{detection limit}$). Subsequently, the suspension was illuminated with a 300 W Xenon lamp, equipped with a cold-mirror 1 (CM1) and a water filter tempered at 303 K. High EG conversion experiments were performed over Rh/TiO_2 using high power UV-LEDs (365 nm) instead of the 300 W Xe-lamp. The evolved gases were analyzed by an online gas chromatograph (Shimadzu, GC 2010 Plus with Ar as carrier gas and a Chromosorb 101 column connected with a MS-5Å column), equipped with a TCD, FID and a methanizer. The concentrations of dissolved gases, in particular CO_2 , were accounted for by applying Henry's law. H_2 production rates were determined by dividing the difference of H_2 amounts between two adjacent data points by the corresponding time interval. Concentrations in the liquid were determined by quantitative ^1H NMR spectroscopy. Liquid samples were withdrawn via a sample valve, filtered with a nylon syringe filter and analyzed.

^1H NMR analysis. A sample of 400 μL was mixed with 400 μL of pH-adjusted internal standard (20 mM 1,3,5-trihydroxybenzene in D_2O , pH adjusted with DCl to 2.7). All experiments were performed at 305 K using an Avance III 500 System (Bruker Biospin, Rheinstetten, Germany) with an UltraShield 500 MHz magnet and a SEI 500 S2 probe head (5 mm, inverse $^1\text{H}/^{13}\text{C}$ with Z-gradient). The measurements were conducted at a magnetic field of 11.75 T. The resonance frequency of ^1H was 500.13 MHz. For all samples, the ^1H NMR spectra were acquired using the one-dimensional NOESY sequence “noesygppr1d.comp” with presaturation of the residual water signal during the relaxation delay and the mixing time using spoil gradients. The relaxation delay was 26 s, and the acquisition time was 4.1 s. Spectra were the result of 64 or 128 scans, with data collected into 32 k data points. Each FID was zero-filled to 64 k data points. Prior to Fourier transformation, an exponential window function with a line broadening factor of 0.2 Hz was applied. The resulting spectra were manually phased, baseline corrected, and integrated using Mestre-C 7.1.0 software package. Chemical shifts were referenced to the internal standard. T_1 , the longitudinal relaxation time, was determined by the inversion recovery pulse sequence method. The sum of

acquisition time and relaxation delay in the quantitative analysis was then adjusted to be equal to or higher than three times T_1 of the slowest relaxing molecule (formic acid). The reaction products were identified according to their specific ^1H NMR chemical shifts verified with measurements of commercial references recorded under the same experimental conditions (SI – Table 1). The amounts of products were determined on the basis of their signal intensities (integrals) referenced to the known molar amount of the internal standard. As the signal intensity of formaldehyde and glyoxal was affected by the water suppression, each compound was respectively calibrated using five to seven calibration solutions. Quantitative gas and liquid phase analysis (detection limit: 0.1 ppm) allowed obtaining closed hydrogen and carbon balances.

Photocatalytic water–gas shift reaction experiments. 75 mg of photocatalyst was suspended in 100 mL water, kept at 288 K. The system was evacuated four times in order to remove O_2 quantitatively and was subsequently filled with 8 mbar of CO and then with Ar up to atmospheric pressure 30 min prior illumination. All other experimental procedures correspond to the above description.

2.4. Catalyst characterization

Elemental analysis. Ga and Zn concentrations were determined by inductively coupled plasma atomic emission spectroscopy (ICP-AES) using a spectroflame-ICP spectrometer (Spectro Analytical Instruments Inc.). Rh concentrations were determined by atomic absorption spectroscopy (AAS) using an Thermo Scientific – SOLAAR M Series AA spectrometer. H–C–N elemental analyses were carried out by the Microanalytical Laboratory at the Technischen Universität München.

Textural properties. Specific surface area and average pore diameter were determined by N_2 adsorption–desorption measurements carried out at 77 K using a PMI automated BET sorptometer. All samples were outgassed at 523 K for 20 h before the measurements. The specific surface area and the average pore diameter were calculated applying the BET and BJH models, respectively.

X-ray diffraction (XRD). XRD-patterns were collected on a STOE STADI-P diffractometer ($\text{Cu-K}_{\alpha 1}$ radiation, $\lambda = 1.54051 \text{ \AA}$, Ge-monochromator) using a Dectris Mythen 1 K detector.

H_2 chemisorption. The catalyst was collected after reaction in order to determine the particle size of the metallic Rh particles which are considered to be obtained by *in situ* photoreduction. The samples were activated in H_2 at 473 K for 2 h. H_2 adsorption (physisorption and chemisorption) was measured over the pressure range from 1 kPa to 15 kPa at 313 K. The sample was outgassed at 313 K for 1 h and a second isotherm was measured in order to determine physisorbed H_2 . The concentration of chemisorbed H_2 was determined by extrapolating the subtracted isotherm to zero H_2 pressure. Mean Rh particle size was calculated assuming half spheres and one atom of hydrogen chemisorbed on one surface atom of Rh.

Diffuse reflectance UV–vis (DR UV–vis) spectroscopy. DR UV–vis measurements were performed with an Avantes Avaspec 2048 spectrometer equipped with a reflection probe (FCR-7UV200-2-ME) with a homemade sample holder. All DR UV–vis spectra are

plotted in the form of Kubelka–Munk function defined as $F(R) = (1 - R)^2 \cdot (2R)^{-1}$ with $R = R_s/R_T$, where R_s is the reflectance of the sample and R_T is the reflectance of Teflon used as a reference.

Transmission and scanning electron microscopy (TEM and SEM). TEM images were recorded on a JEOL JEM-2010 transmission electron microscope operating at 120 kV with a magnification of 200 k. Before measurement, the catalyst sample was ground, suspended in ethanol, and ultrasonically dispersed. Droplets of the suspension were transferred to a copper grid-supported carbon film. The average Rh particle size was calculated from 300 measured particles. SEM images were taken on a JEOL JSM 5900 LV microscope operating at 2.0 kV. The samples were measured without any pretreatment.

X-ray absorption spectroscopy (XAS). X-ray absorption near edge structure (XANES) measurements at the Rh K-edge were conducted at the BM25 beamline of the European Synchrotron Radiation Facility (ESRF). The storage ring was operated at 6 GeV. A Si(111) double crystal monochromator was used and detuned to about 60% of maximum incident intensity in order to minimize contributions from higher harmonics. Experiments were conducted at room-temperature and in fluorescence mode using a 13-element Si(Li) solid-state detector. Photocatalyst samples collected after synthesis were examined in quartz capillaries (2 mm outer diameter, 0.05 mm wall thickness). A Rh foil was placed in between two ionization chambers as a reference for energy calibration of each spectrum, whereas the edge position of Rh(0) was set to 23,220 eV. All spectra represented the average of at least three spectral scans and were normalized to an edge step height of one absorption unit.

2.5. Light intensity measurements

Light intensity measurements were performed with an Avantes Avaspec 2048 spectrometer equipped with a SMA terminated quartz fiber (FC-UV-200-1-ME-SR) equipped with a cosine corrector (CC-UV/Vis). The spectrometer was calibrated using a calibrated light source (AvaLight DH-BAL-CAL).

3. Results and discussion

3.1. Synthesis procedure and physicochemical properties of photocatalysts

The Rh content, particle size and textural properties of the photocatalysts are compiled in Table 1. AEROXIDE® TiO_2 P25 (denoted as TiO_2) is a mixture of anatase (75%, 25 nm) and rutile (25%, 80 nm) and absorbs solely UV-light due to its band gap of 3.1 eV (SI – Fig. 1). Deposition of Rh slightly reduced the pore volume and the specific surface area of the parent TiO_2 , but did not influence the band gap and phase composition. The metal content was 1.0 wt.% and the particle size, derived from H_2 chemisorption was 1.5 nm in good agreement with TEM analysis ($1.7 \pm 0.7 \text{ nm}$, SI – Fig. 2).

The solid solution $(\text{GaN})_{0.86}(\text{ZnO})_{0.14}$ (SI – Fig. 3, SI – Table 2; denoted in the following as GaN:ZnO) exhibited a band gap of

Table 1
Chemical composition, band gap and textural properties of synthesized photocatalysts.

Photocatalyst	Rh content (wt.%)	Rh particle size (nm)	BET surface area ($\text{m}^2 \text{g}^{-1}$)	Pore diameter (nm)	Band gap (eV)
Rh/ TiO_2	1.0	1.5 ^a 1.7 (± 0.7) ^b	44	32	3.1
Rh/GaN:ZnO	1.0	7.8 ^a	8–10	–	2.7

^a H_2 chemisorption.

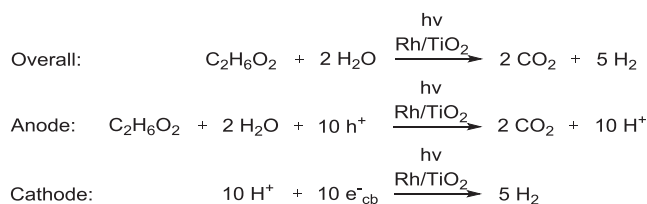
^b TEM (analysis of 300 particles).

2.7 eV (SI – Fig. 1), i.e., it is a visible light absorbing material. HR-SEM images show that primary, nm-sized particles are agglomerated to μm -sized secondary particles (SI – Fig. 4). The surface area of GaN:ZnO was 8–10 $\text{m}^2 \text{g}^{-1}$. The averaged Rh particle size after photoreduction was 7.8 nm (determined from H_2 chemisorption). Different sizes of Rh particles were obtained on TiO_2 and GaN:ZnO because of the differences in the areas available for dispersing the metal. TiO_2 is a mesoporous support with a surface area of 53 $\text{m}^2 \text{g}^{-1}$, whereas GaN:ZnO is a non-porous support with surface area of 8–10 $\text{m}^2 \text{g}^{-1}$.

Normalized XANES spectra obtained at the Rh K-edge for $\text{RhO}_x/\text{TiO}_2$ and $\text{RhO}_x/\text{GaN:ZnO}$ as well as the reference materials are shown in Supporting information, SI – Fig. 5. The Rh K-edges of the two samples indicate a similar oxidation state. The absorption edges as well as near edge absorption fine structure (NEXAFS) with absorption maxima at 23,245 eV and 23,300 eV resemble the Rh_2O_3 reference indicating a predominantly oxidized co-catalyst [28]. We conclude that the H_2 reduced Rh/TiO_2 oxidized under ambient conditions. The NEXAFS absorption maxima around 23,245 eV indicate that Rh on TiO_2 is less oxidized than on GaN:ZnO. Thus, the fresh catalysts consist of mixtures of Rh and RhO_x , the latter being the dominating phase. Under reaction conditions, however, it is hypothesized that RhO_x undergoes *in situ* photoreduction to form metallic Rh, which acts as site for hydrogen recombination to H_2 . Ongoing investigations address the oxidation state of Rh under reaction. For simplicity both catalysts are denoted as Rh/TiO_2 and $\text{Rh}/\text{GaN:ZnO}$ in the following.

3.2. EG photoreforming on 1 wt.% Rh/TiO_2

Kinetics of EG photoreforming. The change in standard free enthalpy of the reaction (ΔG_0) is +8.8 kJ mol^{-1} (SI – Table 3). The complete reaction leads to two equivalents of CO_2 and five



Scheme 1. Photocatalytic ethylene glycol reforming.

equivalents of H_2 (Scheme 1). We consider Rh/TiO_2 (as well as later $\text{Rh}/\text{GaN:ZnO}$) as a micro-electrochemical cell, where Rh co-catalyst acts as the cathode (H_2 evolution site). EG and all intermediates are converted to CO_2 on the anodic semiconductor surface.

The expected reaction products of both redox half reactions H_2 (1580 μmol after 12 h) and CO_2 (573 μmol after 12 h) were detected (Fig. 1A). Formation of small quantities of CH_4 (1.3 μmol after 12 h) besides CO (1.5 μmol after 12 h) was also observed (SI – Fig. 6A).

The H_2 evolution rate decreased with reaction time, which is attributed to the consumption of EG (Fig. 1B). The H_2 to CO_2 -ratio also decreased approaching asymptotically a H_2 to CO_2 -ratio of 3.0 instead of the expected ratio of 2.5 (Fig. 1B). Thus, EG is not stoichiometrically mineralized to CO_2 and one or more organic intermediates remain in the aqueous phase. As EG consumption was not observed in the dark, we conclude that any observed reactivity is caused by light induced reactions (SI – Fig. 6B).

Formaldehyde (478 μmol after 12 h), glycolaldehyde (95 μmol after 12 h) and acetaldehyde (43 μmol after 12 h) were the main intermediates. Acetic acid (3 μmol after 12 h), methanol (5 μmol after 12 h) and formic acid (6 μmol after 12 h) were present as minor products (Fig. 2). The aqueous phase was enriched with HCHO with almost constant rate. In contrast, glycolaldehyde and HCOOH reached constant concentrations after five hours indicating that they were consumed by consecutive reactions. Acetaldehyde, the dehydration product of EG (Scheme 2), was also formed by a light-driven process, because its formation was not observed in the absence of irradiation (SI – Fig. 6B). The two C2-intermediates, glycolaldehyde (2e^- -oxidation product, Scheme 3) and acetaldehyde (dehydration product), formed directly from EG, indicated two parallel reaction pathways (Scheme 4). In order to identify the reaction network of each pathway, glycolaldehyde (Path 1) and acetaldehyde (Path 2) were photoreformed over Rh/TiO_2 as discussed below.

Photoreforming of acetaldehyde over Rh/TiO_2 . Photoreforming of acetaldehyde (Scheme 5) on Rh/TiO_2 was conducted under the same conditions than EG photoreforming. The expected reaction products of both half reactions, H_2 (312 μmol after 12 h) and CO_2 (81 μmol after 12 h), were detected (Fig. 3). The low H_2 evolution rate ($\sim 30 \mu\text{mol h}^{-1}$ vs. $130 \mu\text{mol h}^{-1}$ for EG photoreforming) was attributed to a lower adsorption constant of acetaldehyde compared to EG. Acetic acid, a 2e^- -oxidation product of acetaldehyde reforming, was detected in the liquid phase (197 μmol after 12 h, Scheme 6). Furthermore, the formation of CH_4 (42 μmol after

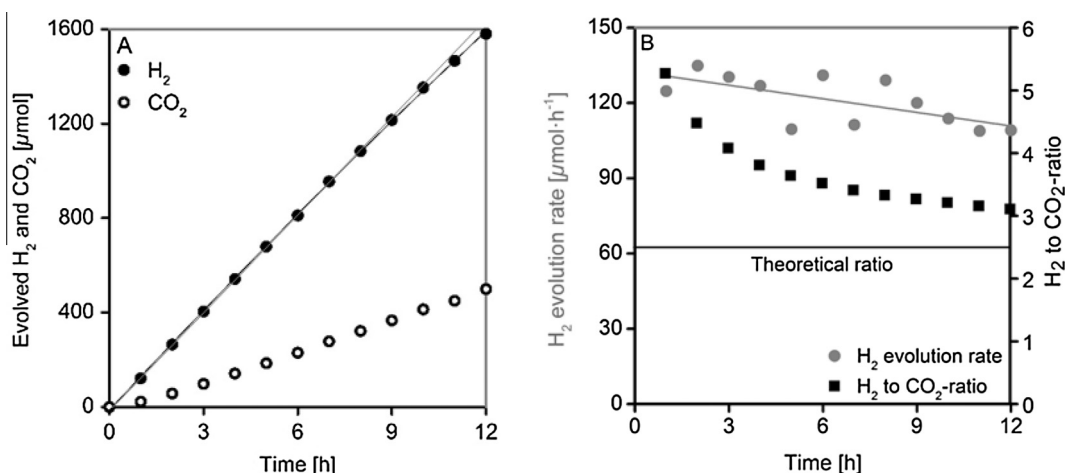


Fig. 1. (A) Course of evolved H_2 and CO_2 . (B) Course of H_2 evolution rate and H_2 to CO_2 -ratio from photocatalytic ethylene glycol reforming (20 mM) over 1 wt.% Rh/TiO_2 (75 mg) dispersed in 100 mL at 288 K and 1 bar using a 300 W Xe-lamp (CM1).

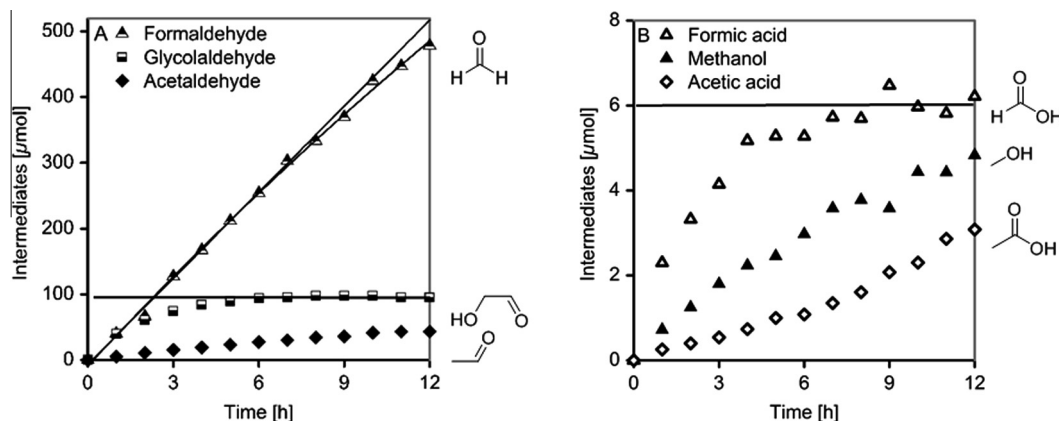
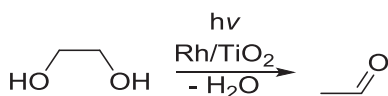
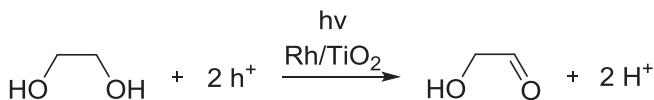


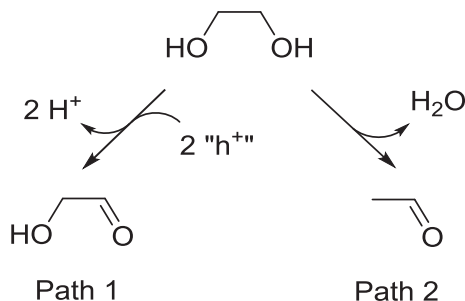
Fig. 2. Course of main (A) and side (B) intermediate formation during ethylene glycol photoreforming (20 mM) over 1 wt.% Rh/TiO₂ (75 mg) dispersed in 100 mL at 288 K and 1 bar using a 300 W Xe-lamp (CM1).



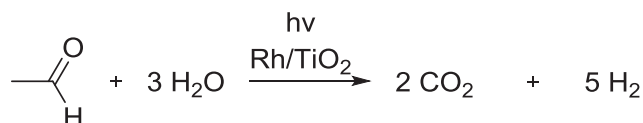
Scheme 2. Dehydration of ethylene glycol to acetaldehyde.



Scheme 3. Oxidation of ethylene glycol to glycolaldehyde.



Scheme 4. Proposed reaction pathways for photocatalytic ethylene glycol reforming over Rh/TiO₂.



Scheme 5. Photocatalytic acetaldehyde reforming.

12 h, Fig. 3B) indicated that CH₃COOH photocatalytically decarboxylates (Photo-Kolbe reaction, Scheme 7) [29]. Note that ethanol had been converted before to mixtures of H₂ and acetaldehyde with only traces of CO₂ and CH₄ [10,30]. Comparison with our results suggests that in that case the weak adsorption of acetaldehyde, compared to ethanol, hindered its conversion to acetic acid and subsequently to CO₂.

CO₂ to CH₄- and H₂ to CH₃COOH-ratios of 1, within the first hour, correspond to those expected from the reactions of Schemes 6 and 7 (acetaldehyde oxidized to acetic acid, which in turn

decarboxylates). With increasing reaction time the ratios of products changed, i.e., the CO₂ to CH₄-ratio was 2 and the H₂ to CH₃COOH-ratio was 1.6 after 12 h. Related to the amount of CH₄ formed, the amount of CO₂ was twice higher than expected, whereas the rates of acetic acid formation declined faster than expected only from the Photo-Kolbe reaction. The differences between the observed amounts of H₂ and CO₂ and the expected ones, based on the stoichiometry of Schemes 6 and 7 and on the amounts of CH₄ and CH₃COOH formed, gave the H₂ to CO₂-ratio of 2. This indicates that the excess of H₂ and CO₂ is produced by oxidative C–C-bond cleavage of acetic acid as shown in Scheme 8.

The network for CH₃CHO oxidation is summarized in Scheme 9. CH₃CHO is oxidized with a low rate to CH₃COOH, which decomposes to CH₄ and CO₂ or is oxidized to CO₂. Thus, the acetic acid and CH₄ observed in EG photoreforming stem from the photoreforming of acetaldehyde (SI – Fig. 6). We cannot speculate on the routes for the photoreforming of acetic acid, because potential intermediates were not observed. It is hypothesized that these intermediates react much faster than acetaldehyde and acetic acid. The slow photoreforming rate of acetic acid indicates that an α -oxygen-functionalized carbon is needed for efficient hole-transfer. The corresponding α -hydroxy functionalized acetic acid (glycolic acid) was photoreformed with high rate (200 $\mu\text{mol H}_2 \text{ h}^{-1}$ at 20 mM, SI – Fig. 7) without decarboxylation.

Photoreforming of glycolaldehyde over Rh/TiO₂. Photoreforming of glycolaldehyde (Scheme 10), the primary product of EG photoreforming (Scheme 4), yielded formaldehyde (1082 μmol after 12 h) and formic acid (65 μmol after 12 h) as main intermediates besides small quantities of acetaldehyde (41 μmol after 12 h) and acetic acid (3 μmol after 12 h) (Fig. 4B). As the amounts of acetaldehyde were very small, this path was considered a side reaction and will not be discussed further at this point.

The formation of formaldehyde and formic acid, on the other hand, suggested that glycolaldehyde was preferentially oxidized via C–C-bond cleavage. Equimolar concentrations of formaldehyde and formic acid were, however, not observed, because HCOOH rapidly decomposed to CO₂ and H₂. Accordingly, the sum of CO₂ and HCOOH were equal to the amounts of HCHO (SI – Fig. 8). The high rate of HCOOH conversion is striking in the light of the negligible conversion of HCHO (see SI – Scheme 1 for the reaction network). The H₂ evolution rate was higher for glycolaldehyde photoreforming (180 $\mu\text{mol H}_2 \text{ h}^{-1}$, 20 mM, Fig. 4A) than for EG reforming (130 $\mu\text{mol H}_2 \text{ h}^{-1}$, 20 mM, Fig. 1B). As glycolaldehyde conversion is initiated by oxidative C–C-bond cleavage, while the OH-group of EG is oxidized to a formyl group, the higher rate of glycolaldehyde conversion than EG conversion suggests that the

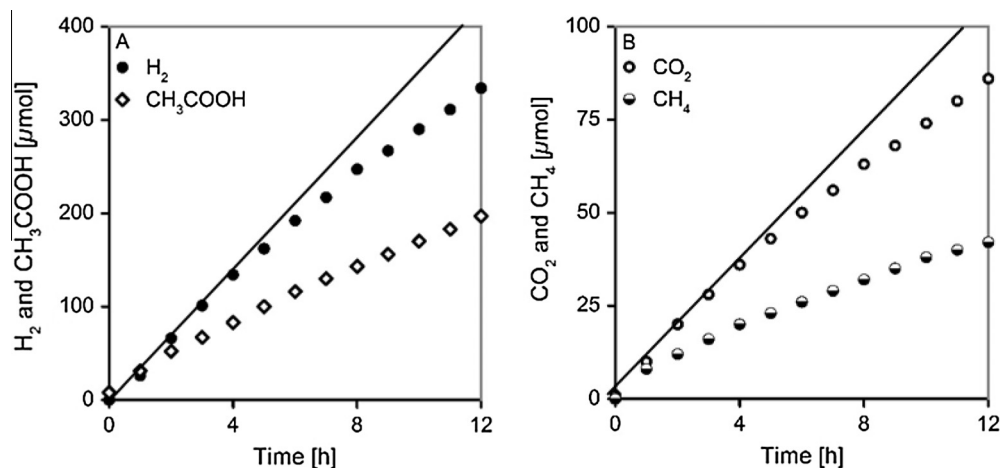
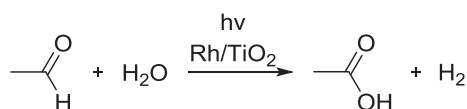
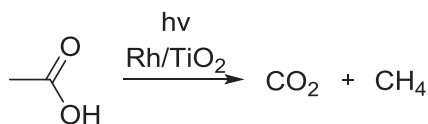


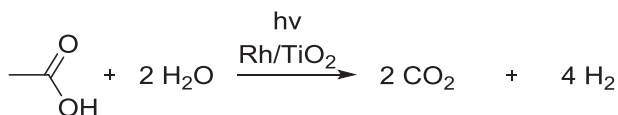
Fig. 3. Comparison of H₂ and acetic acid (A) as well as CO₂ and CH₄ (B) formation courses during acetaldehyde photoreforming (20 mM) over 1 wt.% Rh/TiO₂ (75 mg) dispersed in 100 mL at 288 K and 1 bar using a 300 W Xe-lamp (CM1).



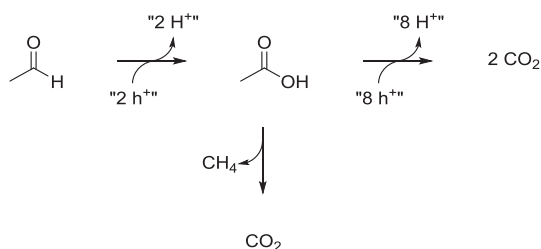
Scheme 6. Anaerobic photo-oxidation of acetaldehyde to acetic acid.



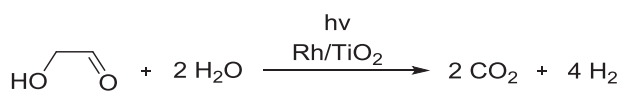
Scheme 7. Photo-Kolbe reaction of acetic acid.



Scheme 8. (Photocatalytic) acetic acid reforming.



Scheme 9. Deduced reaction network for the photocatalytic acetaldehyde photoreforming over Rh/TiO₂.



Scheme 10. (Photocatalytic) glycolaldehyde reforming.

rate of C–C-bond cleavage does not limit the forward rate of polyol photoreforming.

Overall reaction network of EG photoreforming over Rh/TiO₂. Combining the individual reaction pathways allows deducing the

overall reaction network of the photocatalytic EG reforming shown below in [Scheme 11](#). Acetaldehyde was detected with a constant selectivity of 7.1% within 12 h reaction time considering only liquid phase intermediates (SI – [Fig. 9A](#)). Because the reactivity of acetaldehyde was very low and only trace amounts of CH₄ (from decarboxylation of acetic acid) were detected, the formation of CO₂ via conversion of acetaldehyde to acetic acid and subsequent decarboxylation is concluded to be negligible. Thus, Path 2, dehydration of EG to acetaldehyde is only a side reaction. After 12 h, CO₂ accounted for 42% of all converted carbon, the remaining 58% in the liquid phase was predominantly formaldehyde with minor amounts of glycolaldehyde, acetaldehyde and formic acid (SI – [Fig. 9B](#)). Thus, EG is concluded to react with a selectivity of approximately 93% via the formation of the intermediates glycolaldehyde, formaldehyde and formic acid to CO₂ (Path 1).

These results suggest that the pathways proposed by Kondarides et al. [6] for glycerol on 0.5 wt.% Pt/TiO₂ concerning the transformations of the intermediates acetaldehyde and glycolaldehyde are unlikely. The latter intermediate was suggested to oxidize via decarbonylation upon formation of one equivalent of methanol. The absence of CO was explained by photocatalytic water–gas shift, as suggested for alcohol photoreforming over Pd/TiO₂ [31], thermal reforming of EG, [32,33] and electrochemical EG oxidation [34–36].

We can rule out this pathway because of the low rate of the photocatalytic water–gas shift reaction (0.4 μmol H₂·h⁻¹) on 1 wt.% Rh/TiO₂, which is in agreement with the low quantum efficiency of 0.5% reported in the literature [37]. In contrast, for the photocatalytic alcohol reforming typically quantum efficiencies between 20% and 40% for noble metal supported on TiO₂ have been reported and are confirmed in this study [1]. Thus, we conclude that in the present case the C–C-cleavage of glycolaldehyde occurs via a one electron release for each carbon atom leading to the formation of stoichiometric amounts of formaldehyde and formic acid that undergoes dehydrogenation.

Influence of the co-catalyst on the anodic reaction network. Rh nanoparticles, obtained by reduction with H₂, may undergo oxidative disruption after CO adsorption accompanied with the formation of Rh(I)-dicarbonyls, which may influence individual reaction steps [38]. In order to investigate their potential influence on the anodic reaction network, photocatalytic EG reforming was studied on 1 wt.% Pt/TiO₂. Comparison of the selectivities (SI – [Table 4](#), SI – [Fig. 10](#)) shows that the reaction pathways observed on Rh/TiO₂ ([Scheme 11](#)) are identical to the pathways on Pt/TiO₂. Both co-catalysts act only as sites for H₂ evolution.

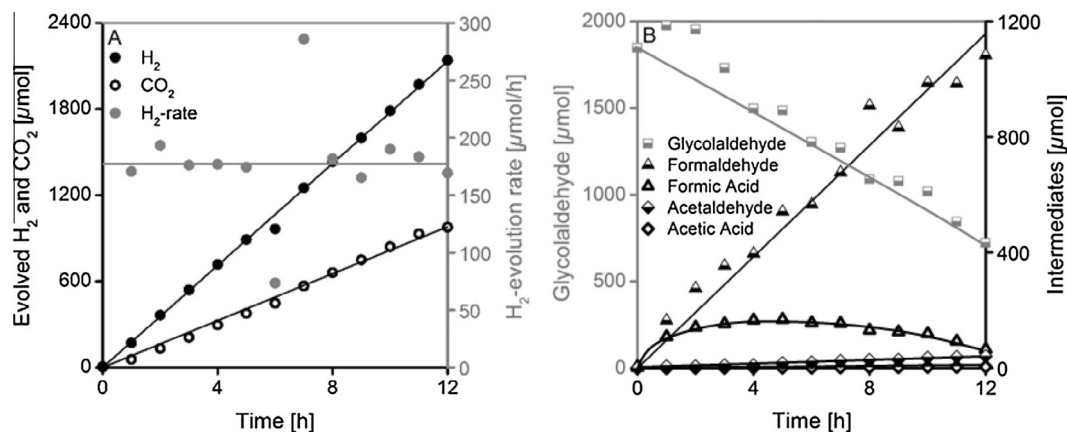
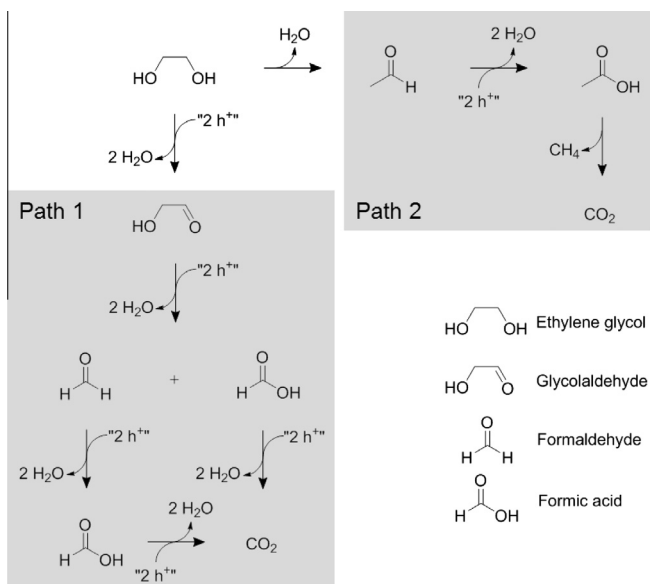


Fig. 4. (A) Course of evolved H₂ and CO₂ as well as H₂ evolution rate. (B) Reactant consumption and intermediate formation during glycolaldehyde photoreforming (20 mM) over 1 wt.% Rh/TiO₂ (75 mg) dispersed in 100 mL at 288 K and 1 bar using a 300 W Xe-lamp (CM1).



Scheme 11. Deduced reaction network for the photocatalytic ethylene glycol reforming (EG#1) over Rh/TiO₂ based on quantitative liquid and gas phase analysis.

Determination of adsorption constants through kinetic modeling. Photoreforming of various C1- and C2-oxygenates (20 mM) yielded different H₂ evolution rates (SI – Fig. 7) [7]. Among these oxygenates, formic acid, oxalic acid, glycolic acid and glyoxylic acid exhibited identical maximum activities of around 200 μmol H₂ h⁻¹. Photoreforming of a 20 mM solution of methanol resulted in an apparent evolution rate of 40 μmol H₂ h⁻¹. However, when the methanol concentration was increased to 2.5 M, we also observed an activity of 200 μmol H₂ h⁻¹. Thus, we hypothesize that the observed H₂ evolution rates depend only on the surface coverage determined by the specific adsorption constant of the oxygenate. This implies that the intrinsic rate constants of the oxidations are only subtly influenced by the nature of the substrate. Indeed, H₂ evolution rates obtained from systematic variations of the initial EG concentration suggest that the photocatalytic rate follows a Langmuir adsorption based rate Eq. (1) (SI – Fig. 11).

$$\frac{dc_i}{dt} = \frac{k^{app} \cdot K_i^{L,app} \cdot c_i}{1 + \sum_{i=1}^n K_i^{L,app} \cdot c_i} \quad (1)$$

where dc_i/dt is the reaction rate of reactant i (mM min⁻¹), k^{app} is the maximum apparent rate constant of the component i (mM min⁻¹), $K_i^{L,app}$ is the apparent Langmuir adsorption constant of component i (L mmol⁻¹) and c_i is the concentration of component i (mmol L⁻¹). The denominator describes competitive adsorption of n chemical species.

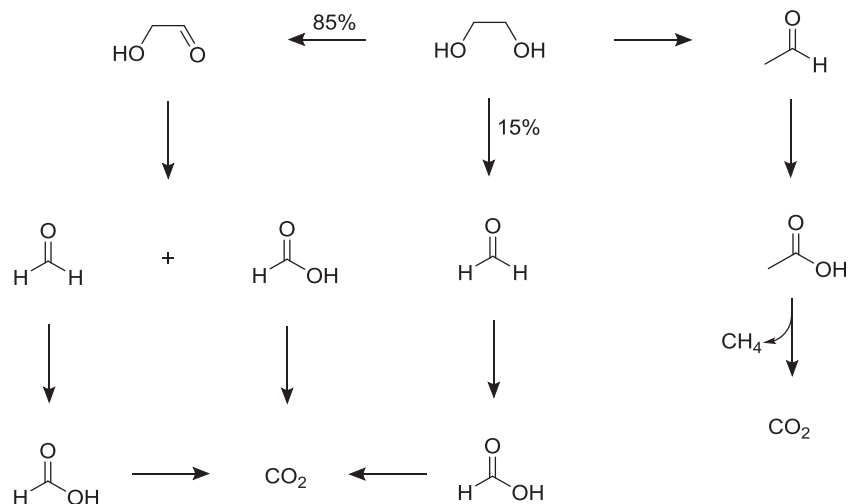
The Langmuir model is compatible with a disrupted adsorption kinetic model (Eq. (2)) which considers the light dependence of the apparent Langmuir adsorption constants [23].

$$\frac{dc_i}{dt} = \frac{k^{app} \cdot K_i^{DA,app} \cdot c_i}{1 + \sum_{i=1}^n K_i^{DA,app} \cdot c_i} \quad (2)$$

In this equation dc_i/dt denotes the reaction rate of reactant i (mM min⁻¹), k^{app} is the maximum apparent rate constant of the component i (mM min⁻¹), $K_i^{DA,app}$ is the apparent adsorption constant of component i (L mmol⁻¹) and c_i is the concentration of component i (mmol L⁻¹). The denominator describes competitive adsorption of n chemical species. Details of the derivation of the kinetic model are given in Supporting information and in Ref. [24]. The apparent adsorption constant $K_i^{DA,app}$ (dimensionless) may be obtained from $K^{DA,app} \cdot c_s$, where $K^{DA,app}$ is multiplied with the solvent molar concentration c_s (here: water, 55,508 mmol L⁻¹) [39].

In order to obtain general and reliable fitting parameters, the apparent adsorption constants were determined by fitting the photoreforming of several compounds. The reactions included methanol photoreforming, which contained formaldehyde and formic acid as intermediates [16]. The maximum rate of 200 μmol H₂ h⁻¹ was used as constraint. The reaction networks of glycolaldehyde and EG photoreforming were taken as basis to establish the system of differential equations with the form of Eq. (2). The reaction network in SI – Scheme 2 was used for methanol reforming. These boundary conditions led to adsorption constants of the reactants and intermediates involved in methanol and glycolaldehyde photoreforming that agree very well with the experimental data (SI – Fig. 12, and SI – Fig. 13, respectively). In contrast, the introduction of an additional reaction pathway was required in order to obtain an acceptable agreement for the data of EG reforming (SI – Fig. 14), i.e., oxidative C–C-cleavage of EG to two equivalents of formaldehyde (Scheme 12).

Table 2 indicates the validity of this approach and the transferability of the results, as similar apparent adsorption constants, K^{app} , were obtained for each oxygenate in different photoreforming reactions. The determined values compare well with values reported in previous studies (SI – Table 5) [40–42]. The good fitting of the experimental data with the kinetic model confirms that the photocatalytic rates depend primarily on surface coverage.



Scheme 12. Deduced reaction network for the photocatalytic ethylene glycol reforming (EG#2) over Rh/TiO₂ based on quantitative liquid and gas phase analysis and kinetic fitting.

Table 2

Comparison of fitted adsorption constants (K^{app} , $\cdot 10^4$) of several C1- and C2-oxygenates from various photoreforming reactions at 288 K.

Probe molecule	Photoreforming reaction		
	Ethylene glycol	Glycolaldehyde	Methanol
Ethylene glycol	0.27	–	–
Glycolaldehyde	3.6	5.1	–
Methanol	–	–	0.068
Formaldehyde	0.34	0.26	0.32
Formic acid	77	49	48

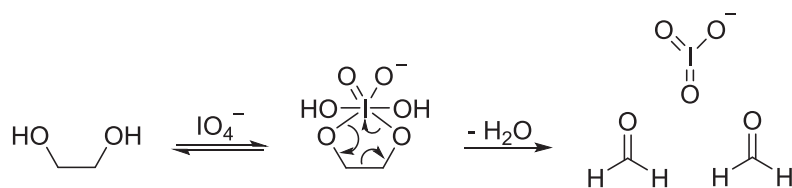
It should be highlighted that the apparent adsorption constant of formaldehyde is two orders of magnitude smaller than that of formic acid. Thus, we conclude that the low adsorption constant of formaldehyde causes its accumulation in the liquid phase during photoreforming reactions of EG, glycolaldehyde and methanol.

On the elementary steps of the reaction network. All anodic oxidations are attributed to direct electron transfer from the oxygenate to the hole and/or an indirect $\cdot\text{O}(\text{H})$ -radical driven oxidation. The existence and relative importance of these two pathways on TiO₂ has been extensively investigated [43–48]. Modeling of the oxidation kinetics in the present study shows that EG is oxidized to formaldehyde *via* C–C-bond cleavage (15%) as well as to glycolaldehyde (85%). The latter product is hypothesized to be generated *via* an $\cdot\text{O}(\text{H})$ -radical mediated mechanism following a Fenton's reagent like chemistry. $\cdot\text{O}(\text{H})$ -radicals abstract a $\cdot\text{H}$ -atom in α -position; the resulting carbon centered radical is further oxidized to glycolaldehyde by losing a further $\cdot\text{H}$ atom. A Fenton's reagent mediated degradation of EG does not show HCHO formation, because the diol is gradually oxidized to oxalic acid before C–C-bond cleavage [49,50]. Thus, oxidative C–C-bond rupture of EG to formaldehyde is concluded to be associated with a direct electron transfer in close resemblance to the reaction mechanism of a

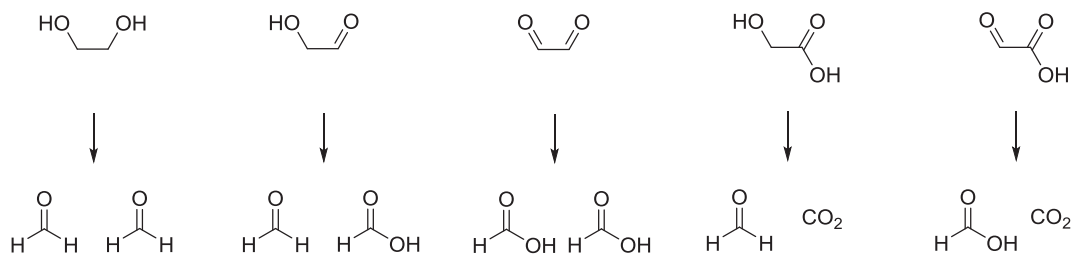
Malaprade periodic acid oxidation reaction. In these reactions, periodic acid ($E^0(\text{IO}_4^-/\text{IO}_3^-) = 1.60$ V at 298 K) [51] and EG form a five-membered cyclic ester. The C–C-bond is formally cleaved upon one electron transfer from each carbon atom to the iodine which is reduced to iodic acid (Scheme 13) [52]. Photoreforming of any oxygenate functionalized with a sp^2 -hybridized α -oxygen over Rh/TiO₂ occurs exclusively *via* oxidative C–C-cleavage as neither hydroxy- nor formyl-groups are oxidized. The intermediates during photoreforming of these oxygenates, i.e., glyoxal, glycolic acid and glyoxylic acid, equaled the expected reactivity of the Malaprade oxidation reaction (Scheme 14). This implies that oxidation of sp^2 -hybridised α -oxygen functionalized C2-oxygenates occurs *via* direct hole-transfer. The α -carbon atom must be functionalized with an oxygen containing group. In contrast, acetaldehyde is oxidized to acetic acid and C–C-cleavage occurs *via* photon induced decarboxylation (Photo-Kolbe reaction).

As oxygenates are oxidized *via* direct or indirect hole transfer, at least two different adsorption sites must exist. We hypothesize that these two active sites are (i) oxygen atoms of terminal OH-groups and (ii) sites containing two Ti cations and a bridging oxygen in agreement with Refs. [12,53]. Scheme 15 schematically shows the surface structure of TiO₂ denoted as (I), which is subsequently described as $\text{Ti}(\text{OH})_{\text{T}}(\text{O})_{\text{B}}$ (Schemes 15 and 16).

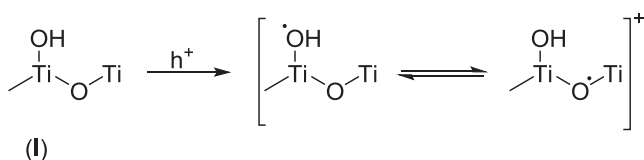
Titanium K-edge XANES studies [54] have shown that for small TiO₂ nanoparticles (~ 46 Å), dispersed in aqueous polyol solutions like EG, the coordination of unsaturated surface Ti atoms change almost quantitatively from square pyramidal to octahedral. These structural changes suggest that α -oxygen functionalized oxygenates chemisorb as chelating agents at the TiO₂-surface [54]. Thus, the coordinatively unsaturated Ti(IV)-ion in the $\text{Ti}(\text{OH})_{\text{T}}(\text{O})_{\text{B}}$ species is proposed to be a typical adsorption site for α -oxygen functionalized oxygenates, which catalyzes the selective C–C-cleavage of sp^2 -hybridized α -oxygen functionalized C2-oxygenates.



Scheme 13. Mechanism for cleavage of ethylene glycol with periodate.



Scheme 14. Expected products of the oxidation of C2-oxygenates with periodate.



Scheme 15. Schematic view of shallow surface trapped hole on TiO₂.

Upon coordination with EG the Ti(OH)_T(O)_B site transforms to energetically deeper surface hole traps, Ti(OR)_T(O)_B (II) (Scheme 16), which may allow direct hole transfer [12]. Upon occurrence, an alkoxy-radical (III) is formed, which may be oxidized by a second hole or may undergo direct β-C–C-cleavage. Under experimental conditions, the time between two photons reaching a TiO₂ particle ranges from 1 to 7 ms (SI – Fig. 15, SI – Table 6). For the least reactive *t*-alkoxy radical a rate constant for the β-scission of approximately $2 \cdot 10^3 \text{ s}^{-1}$ is determined at 313 K [55]. Further stabilization of the resulting ·CH_xO_y(H)-radical by adjacent lone-pairs of the oxygen would lead to even faster decomposition of species (III). Therefore, it is highly probable that the rate for β-scission is significantly higher than the rate for a second hole transfer. Indeed, preferential β-C–C-bond cleavage has been shown for free cyclic β-hydroxy alkoxy radicals upon formation of a linear di-aldehyde, demonstrating the rate enhancement by an adjacent oxygen lone pair stabilized radical [56]. In addition, rapid C–C-rupture has been observed for β-hydroxyalkoxy and other oxygen substituted alkoxy radicals with small activation energies (29–40 kJ mol⁻¹) in the gas phase [57].

After β-C–C-cleavage of radical (III) (Scheme 16), formaldehyde and a ·CH₂O(H)-radical (IV) are formed. The latter is expected to readily hydrolyze under acidic conditions. Due to the large negative potential of the ·CH₂O(H)-radical ($E^0(\text{CH}_2\text{O}/\text{CH}_2\text{OH}) = -0.97 \text{ V}$

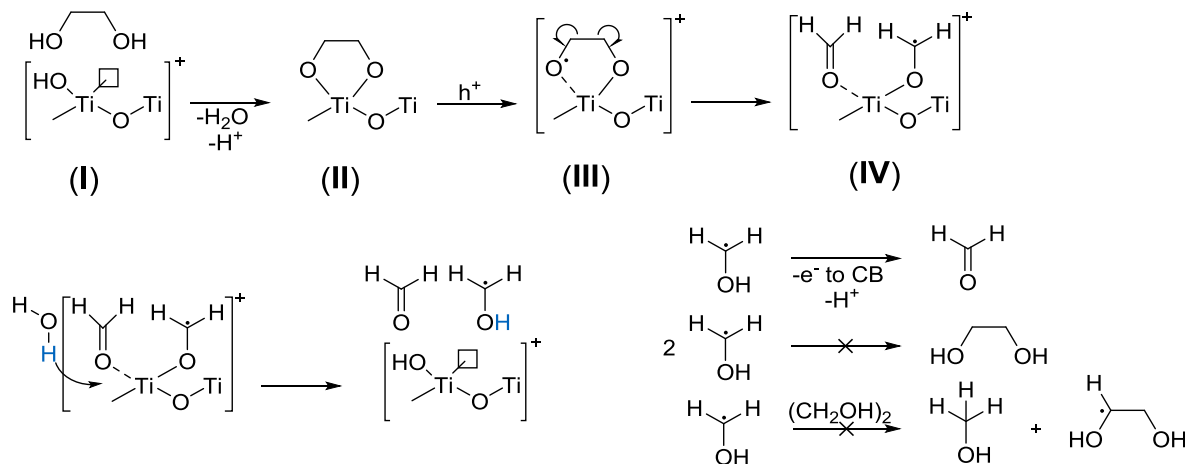
vs. NHE) [58] an electron is injected into the conduction band of TiO₂. This phenomenon (current-doubling), has been extensively studied for methanol as well as various C1- and C2-oxygenates [59–61]. It requires carbon-centered radicals, that in case of a direct hole transfer are only formed after β-C–C-cleavage.

For methanol and EG photoreforming, the same intermediate radical (·CH₂OH) is formed. The absence of EG during glycolaldehyde photoreforming and the small rate of methanol photoreforming allows us to conclude that ·CH₂OH-radicals are efficiently oxidized by current-doubling (Scheme 16). Our proposal is in line with aerobic oxidation studies of glycerol, [12] where a ·CHROH-radical (R = H or CH₂OH) is suggested as an intermediate. In the case of aerobic oxidation, the ·CHROH-radical reduces oxygen.

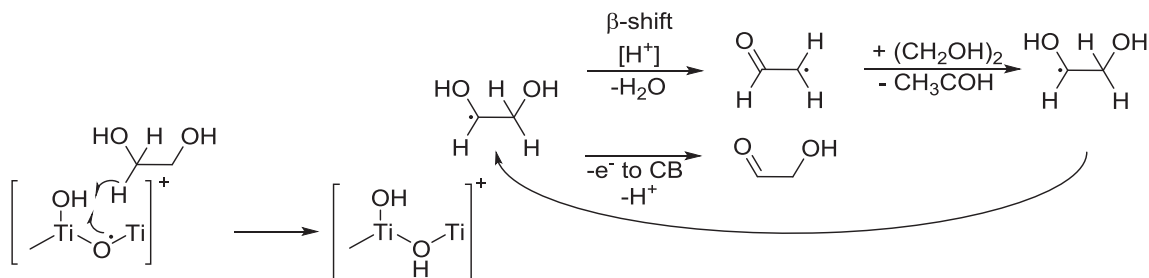
The second site for the conversion of EG is postulated to be a Ti(OH)(O·) shallow surface hole trap (Scheme 15 right, Scheme 17). On these sites, a ·CHOHCH₂OH-radical is formed upon H-atom abstraction. Because of its reductive potential, it can inject an electron into the conduction band of TiO₂ being oxidized to glycolaldehyde. EPR experiments showed that ·CHOHCH₂OH-radicals also can undergo acid-catalyzed β-H-shift (pH < 3) with subsequent dehydration upon formation of a carbon-centered acetaldehyde radical [62]. This carbon-centered radical can abstract an H-atom from another EG molecule leading to acetaldehyde. In homogeneous phase (pH < 3) the rate constant of dehydration is determined as $7 \cdot 10^5 \text{ s}^{-1}$, which is orders of magnitude slower than the acid-catalyzed β-H-shift [62].

These studies show, that the light driven dehydration of EG (Scheme 11, pathway 2) is only a side reaction. Thus, e⁻-injection of the ·CHOHCH₂OH-radical into the conduction band is kinetically preferred compared to the acid-catalyzed β-H-shift of the radical connected with dehydration.

Origin of CO formation. CO evolution was observed during C1- and C2-oxygenate photoreforming on Rh/TiO₂, with the exception



Scheme 16. Proposed anodic oxidation mechanism for C2-oxygenates adsorbing on Ti^{IV}-OH-sites.



Scheme 17. Proposed anodic oxidation mechanism for C2-oxygenates interacting with Ti(OH)(O) shallow surface hole traps.

of oxalic acid. The formation rate of CO strongly depended on the nature of the oxygenate (SI – Fig. 16). High concentrations of CO evolved from oxygenates with formyl groups (e.g., glycolaldehyde) compared to those not containing formyl groups (e.g., EG) suggest that CO is formed by decarbonylation in agreement with proposals in the cases of electrocatalytic EG oxidation [63] and thermal aqueous phase reforming of EG [33].

In order to explore the origin of CO formation during photoreforming, each intermediate has been reacted over parent TiO₂. Due to the absence of the Rh co-catalyst, H₂ evolution was kinetically hindered. Thus, CO evolved from the reactant and not from an intermediate. Very little amounts of CO were detected from EG (1.4 μmol CO after 5 h), glycolaldehyde (9.0 μmol CO after 5 h) and formaldehyde (4.8 μmol CO after 5 h). In contrast, pronounced CO evolution occurred in case of formic acid photoreforming (216 μmol CO after 5 h). Thus, CO formation is concluded to be caused by dehydration of formic acid, in agreement with results from methanol photoreforming on Pt/TiO₂ [13–16,64]. In consequence, the CO evolution followed formic acid formation (SI – Fig. 17). Indeed, there is a linear correlation between the surface coverage of formic acid (determined from the apparent adsorption constant) and the rate of CO formation (SI – Fig. 18). We emphasize at this point that both dehydrogenation and dehydration of formic acid are light-driven reactions. The active sites for the dehydration of formic acid are hypothesized to be formed only during the reaction, because an induction period was observed for CO evolution (SI – Figs. 6A and 19B).

3.3. EG photoreforming over 1 wt.% Rh/GaN:ZnO

Kinetics of EG and glycolaldehyde photoreforming over 1 wt.% Rh/GaN:ZnO. GaN:ZnO is much more labile against reduction than

TiO₂. Thus, it had to be post-calcined in static air in order to remove Zn(0) surface defects, which act as electron–hole recombination centers [19]. This led to a three-fold higher photocatalytic activity compared to non post-calcined GaN:ZnO. During the photoreforming experiments, H₂ (698 μmol after 47 h) and CO₂ (237 μmol after 47 h), were detected (Fig. 5A). A constant amount of oxygen (~2–4 μmol) was also observed during the experiments. This is attributed to the activity of Rh/GaN:ZnO for overall water-splitting (vide infra). The H₂ evolution rate, starting from 35 μmol H₂·h⁻¹, steadily decreased and stabilized at around 12 μmol H₂·h⁻¹. The lower level after this decrease corresponds to the photocatalytic activity of non post-calcined GaN:ZnO. Thus, we conclude that Zn(0) surface defects reappear during photoreforming. As the deactivation was observed for any oxygenate photoreformed over Rh/GaN:ZnO, it is concluded to be caused by the presence of H₂ or conduction band electrons rather than being induced by a specific surface chemistry of an organic reactant.

The formation rate of CO decreased over time as manifested by the steadily rising H₂ to CO ratio (Fig. 5B) (note that the opposite trend was observed over Rh/TiO₂). The absence of CH₄ indicates that EG is not dehydrated to acetaldehyde, the precursor of acetic acid and concomitant CH₄ (vide supra). As acetaldehyde is induced by surface-bound ·O(H)-radical over Rh/TiO₂, the absence of dehydration pathways is a direct consequence of the less positively located valence band of GaN:ZnO. In addition, an increased degree of mineralization was observed on Rh/GaN:ZnO (H₂ to CO₂ = 2.9; H₂: 698 μmol) compared to Rh/TiO₂ (H₂:CO₂ = 3.5, H₂: 757 μmol). In the liquid phase, glycolaldehyde (138 μmol after 47 h) and formaldehyde (57 μmol after 47 h) as well as a variety of C2-oxygenates, i.e., glycolic acid, glyoxal and glyoxylic acid (all <1.5 μmol after 47 h) were identified (Fig. 6). Thus, photoreforming of glycolaldehyde was explored to probe whether these higher

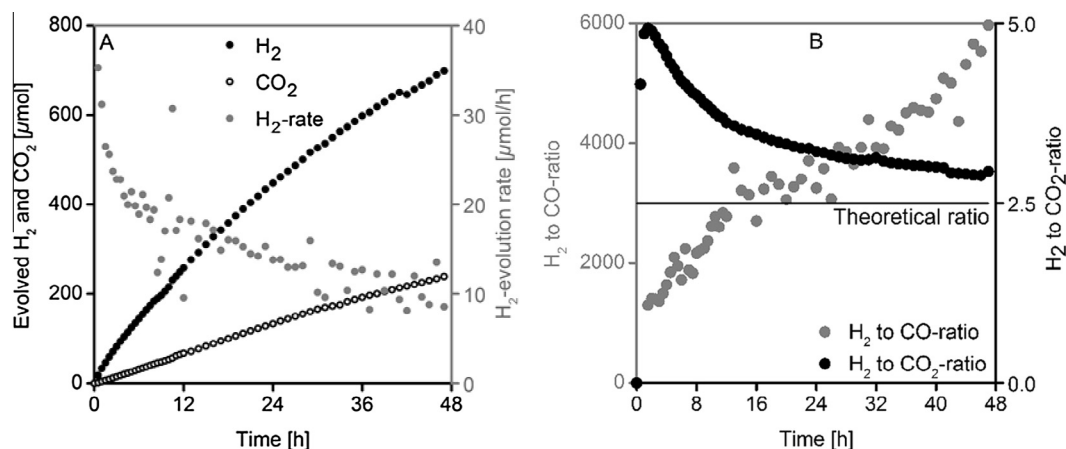


Fig. 5. (A) Course of evolved H₂ and CO₂ as well as H₂ evolution rate. (B) H₂ to CO-ratio and H₂ to CO₂-ratio during ethylene glycol photoreforming (20 mM) over 1 wt.% Rh/GaN:ZnO (75 mg) dispersed in 100 mL at 288 K and 1 bar using a 300 W Xe-lamp (CM1).

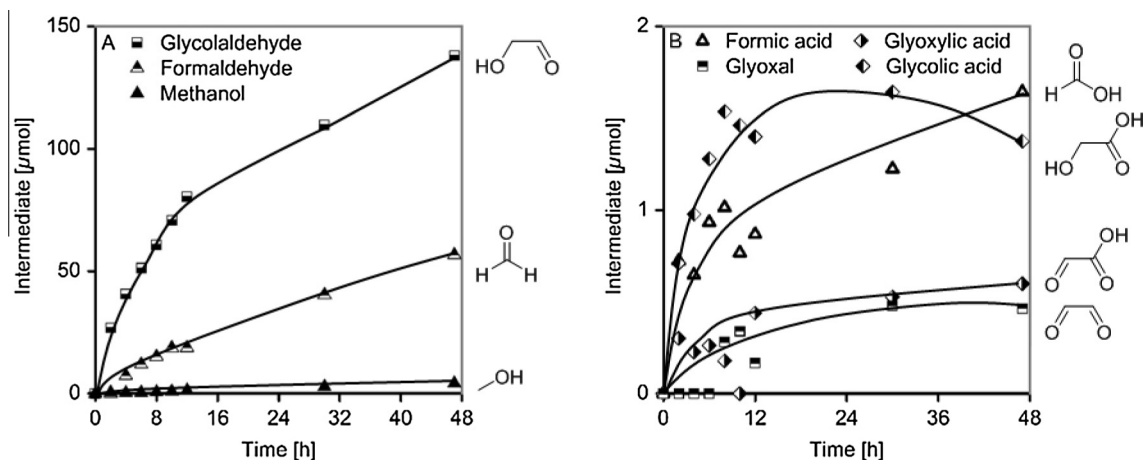


Fig. 6. Course of main (A) and side (B) intermediate formation during ethylene glycol photoreforming (20 mM) over 1 wt.% Rh/GaN:ZnO (75 mg) dispersed in 100 mL at 288 K and 1 bar using a 300 W Xe-lamp (CM1).

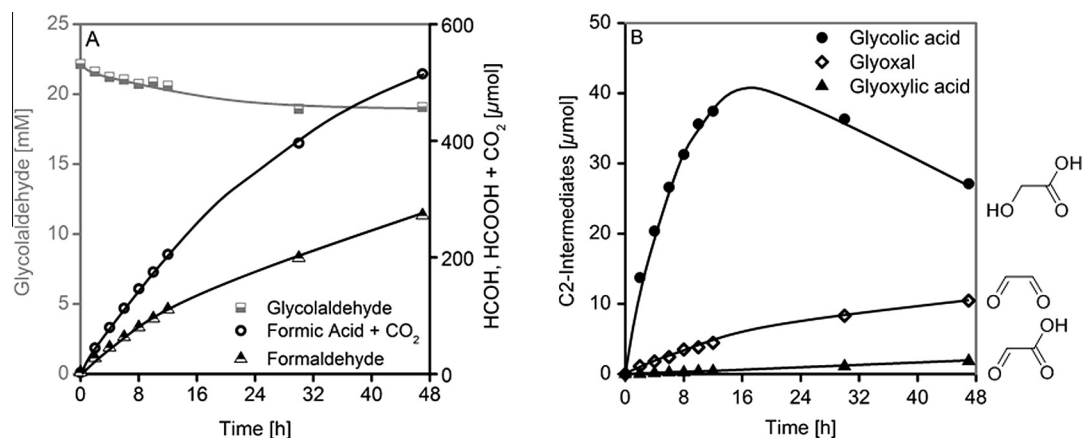


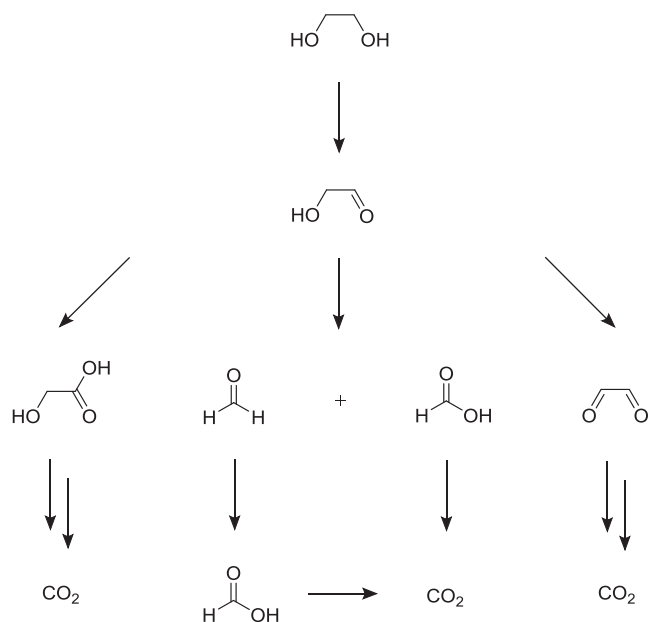
Fig. 7. (A) Consumption of glycolaldehyde and comparison of amounts of detected formaldehyde and totalized amounts of detected formic acid and CO₂. (B) Course of C₂-intermediate formation during glycolaldehyde photoreforming (20 mM) over 1 wt.% Rh/GaN:ZnO (75 mg) dispersed in 100 mL at 288 K and 1 bar using a 300 W Xe-lamp (CM1).

oxidized C₂-oxygenates are part of the main degradation pathways. Formaldehyde was the main intermediate, suggesting that glycolaldehyde was oxidized via C–C-cleavage to formaldehyde and formic acid. In contrast to Rh/TiO₂, the amounts of formic acid and CO₂ exceeded the amounts of detected formaldehyde (Fig. 7A). This was attributed to additional pathways, because the higher oxidized C₂-products (e.g., glyoxal (10 μmol after 47 h) or glycolic acid (27 μmol after 47 h)) showed that glycolaldehyde was not selectively converted to formaldehyde and formic acid (Fig. 7B). The small concentration of formic acid, glycolic acid, and glyoxylic acid during EG photoreforming (Fig. 6) was attributed to high adsorption constants in analogy to the observations over Rh/TiO₂.

Impact of the potential on photoreforming – catalysis on Rh/GaN:ZnO. Materials for visible-light driven photocatalytic H₂ evolution have a less positive valence band than TiO₂ (e.g., on GaN:ZnO, VB_{GaN:ZnO}: +1.72 V vs. NHE) [65]. In the case of GaN:ZnO, surface-bound hydroxyl radical mediated pathways are, therefore, excluded (E⁰(·OH,H⁺/H₂O) = +2.72 V vs. NHE) [66]. Rh/GaN:ZnO is, however, active for the overall water-splitting reaction, implying that additional oxidizing species, such as free hydroxyl- (·OH) or perhydroxyl-radicals (·OOH), are formed. Thus, the lower anodic potential and additional oxidizing species induce a different anodic reaction network compared to Rh/TiO₂.

The proposed reaction network for the photoreforming of EG over Rh/GaN:ZnO is presented in Scheme 18. The presence of higher oxygenated products of glycolaldehyde conversion over Rh/GaN:ZnO implies that additional mechanisms other than direct hole transfer exist. As no surface-bound ·O(H)-radicals can be formed, free perhydroxyl-radicals or hydroxyl-radicals resulting from reduced oxygen have to be responsible for the oxidation of ethylene glycol to glycolaldehyde and subsequently to glyoxal or glycolic acid. Thus, the free radicals open additional reaction pathways and glycolaldehyde is converted to higher oxidized C₂-oxygenates. The generation of glyoxal and glyoxylic acid is of special interest as those species do not form formaldehyde (drawback for further applications due to its toxicity) after C–C-cleavage. In contrast, on Rh/TiO₂, α-oxygen functionalized sp²-hybridized C₂-oxygenates interact selectively with terminal Ti^{IV}-OH groups and are oxidized via C–C-cleavage.

Comparison of CO evolution during EG photoreforming over Rh/TiO₂ and Rh/GaN:ZnO. Photoreforming of EG over Rh/TiO₂ generates H₂ containing 975 ppm CO after 12 h, whereas a very CO-poor H₂ stream (180 ppm CO after 47 h) is obtained for the same reaction on Rh/GaN:ZnO (Fig. 8). The course of CO evolution also strongly differs for these two photocatalysts. A steadily rising CO content is observed on Rh/TiO₂, whereas the opposite was observed on



Scheme 18. Deduced reaction network for photocatalytic ethylene glycol reforming over Rh/GaN:ZnO based on quantitative liquid and gas phase analysis.

Rh/GaN:ZnO. After some accelerated initial formation, the CO evolution rate stabilizes on a very modest level ($\sim 0.1 \mu\text{mol CO}\cdot\text{h}^{-1}$). This low rate of CO formation is explained by the very low concentration of its intermediate precursor formic acid, i.e., ($\sim 15 \mu\text{M}$) in contrast to Rh/TiO₂ ($\sim 60 \mu\text{M}$).

3.4. Challenges for a clean EG photoreforming process

Formaldehyde and CO, undesired by-products for potential applications, were observed during EG photoreforming over Rh/GaN:ZnO and Rh/TiO₂. Thus, an experiment with increased photon flux on Rh/TiO₂ was performed in order to verify the course of both compounds at high EG conversions. The EG consumption followed first order kinetics (Fig. 9A) because the chosen starting concentration (20 mM) led to a surface coverage in the Henry's regime (SI – Fig. 11). First order kinetics along the whole conversion range proved that neither increasing CO concentration nor acetic acid (SI – Table 7, SI – Fig. 19A), which is converted at slow rate, adsorb in appreciable concentration on cathode or anode.

During the first four hours of the experiment, almost equivalent amounts of formaldehyde (884 μmol) and CO₂ (973 μmol) were formed (Fig. 9B). At this point, stoichiometric amounts of EG and formaldehyde were present and formation rate equaled the consumption rate. When most of the EG was converted (>85%), the

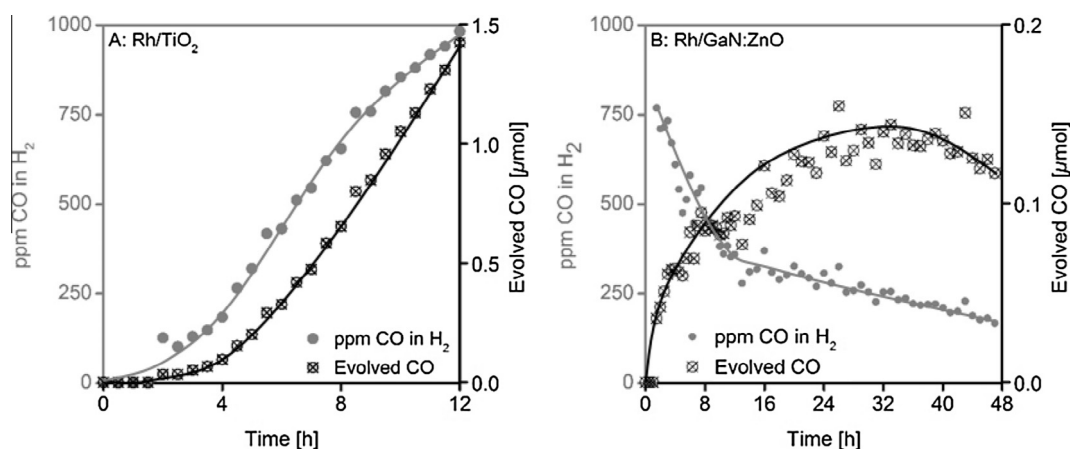


Fig. 8. Course of CO-evolution and CO-content in evolved H₂ for photocatalytic ethylene glycol reforming over Rh/TiO₂ (A) and Rh/GaN:ZnO (B).

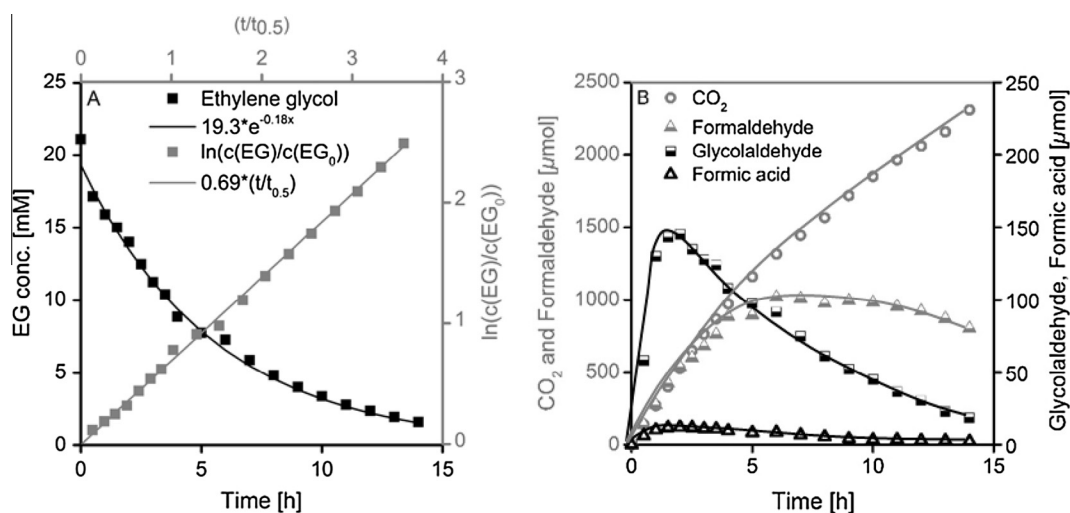


Fig. 9. (A) Ethylene glycol consumption and determination of reaction order. (B) Course of the main intermediates and CO₂ for ethylene glycol photoreforming (20 mM) over 1 wt.% Rh/TiO₂ (75 mg) dispersed in 100 mL at 288 K and 1 bar using 14 10.4 W UV-LEDs, operated at 14.8 V, 400 mA.

concentration of formaldehyde (~ 10 mM) declined. The decreasing competition of other reactants allowed a higher surface concentration of formaldehyde. Due to the small adsorption constant of formaldehyde, however, very low H_2 evolution rates were observed during the reaction even at high EG conversions ($\sim 200 \mu\text{mol } H_2 \cdot h^{-1}$ vs. initially $1100 \mu\text{mol } H_2 \cdot h^{-1}$). The CO content in relation to the evolved H_2 increased up to 5500 ppm before stabilization. The induction period (SI – Fig. 19B) suggests that the active centers are formed during the illumination. In order to decrease CO formation, EG has to be selectively oxidized to oxalic acid which decarboxylates without CO formation.

4. Conclusions

Photoreforming of ethylene glycol (EG) has been found to be a process, in which the diol acts as sacrificial reductant at the anode to enable the reduction of H^+ . The anodic half reaction occurs *via* two pathways on Rh/TiO₂. The minor pathway proceeds *via* dehydration of EG to acetaldehyde, which is subsequently oxidized to acetic acid, which undergoes Photo-Kolbe reaction. In the dominant pathway EG is oxidized to glycolaldehyde or formaldehyde (*via* oxidative C–C-cleavage), with selectivities of 85% and 15%, respectively. Glycolaldehyde is subsequently converted *via* oxidative C–C-cleavage to formaldehyde and formic acid. Formaldehyde, on the other hand, oxidizes to formic acid, which dehydrogenates to CO₂. The sites proposed for the oxidative C–C-cleavage are terminal Ti^{IV}–OH groups, where the adsorbate is oxidized to an alkoxy-radical upon β -C–C-cleavage. Compounds with a sp^2 -hybridized α -oxygen interact with this reaction site converting to products that correspond to a Malaprade oxidation chemistry. On [Ti–O–Ti]⁺ oxidation occurs by abstracting an H-atom from the oxygenate producing a carbon centered radical, which is further oxidized causing current-doubling. CO evolves during the photoreforming of all C1- and C2-oxygenates (with the exception of oxalic acid).

The linear dependence of the surface coverage of formic acid and the rate of CO formation shows that the light-driven dehydration of formic acid is the source of CO. Identical, maximum H_2 evolution rates for the photoreforming of various C2-oxygenates, imply that the rates are independent of the nature of the reactant and the specific transformation of functional group, and C–C-cleavage under our reaction conditions. Together with the good fit of the experimental data to a Langmuir-type kinetic model led to conclude that H_2 evolution rates mainly depend on the concentration and adsorption strength of the specific oxygenate.

In the case of the EG photoreforming over Rh/GaN:ZnO the main conversion occurs *via* glycolaldehyde (as observed over Rh/TiO₂). Additional pathways *via* higher oxidized C2-oxygenates are induced by oxidizing radicals, e.g., $\cdot OH$, $\cdot OOH$, formed from oxygen due to the water-splitting reaction on Rh/GaN:ZnO. These new pathways avoid formaldehyde formation. Thus, while alcohols such as ethylene glycol can be readily oxidized at the photoanode, under the present conditions formaldehyde accumulates in the aqueous phase due to its small adsorption constant until all other compounds are consumed. Dehydration of the intermediate formic acid leads to considerable contents of CO in the H_2 produced.

Acknowledgments

We would like to thank the Federal Ministry of Education and Research (BMBF) for financial support (project no. 01RC1106A). Additionally, we would like to thank Clariant for productive discussions within the framework of MuniCat and the iC^4 PhotoCOO project. The authors would like to thank ESRF in Grenoble, France, for

providing beam time at the BM25 station for XAFS experiments. K.E.S. gratefully acknowledges financial support by the Fond der Chemischen Industrie (FCI). The authors thank Kazuhiro Takanabe for fruitful discussions and scientific advice. We thank Xaver Hecht for technical support, Christine Schwarz for assistance during NMR experiments, and Miriam Wehrle for her contributions to the graphical abstract.

Appendix A. Supplementary material

Supplementary data associated with this article can be found, in the online version, at <http://dx.doi.org/10.1016/j.jcat.2016.02.021>.

References

- [1] K. Shimura, H. Yoshida, *Energy Environ. Sci.* 4 (2011) 2467–2481.
- [2] X.B. Chen, S.H. Shen, L.J. Guo, S.S. Mao, *Chem. Rev.* 110 (2010) 6503–6570.
- [3] F. Dionigi, P.C.K. Vesborg, T. Pedersen, O. Hansen, S. Dahl, A.K. Xiong, K. Maeda, K. Domen, I. Chorkendorff, *J. Catal.* 292 (2012) 26–31.
- [4] D.I. Kondarides, V.M. Daskalaki, A. Patsoura, X.E. Verykios, *Catal. Lett.* 122 (2008) 26–32.
- [5] G.N. Nomikos, P. Panagiotopoulou, D.I. Kondarides, X.E. Verykios, *Appl. Catal. B* 146 (2014) 249–257.
- [6] P. Panagiotopoulou, E.E. Karamerou, D.I. Kondarides, *Catal. Today* 209 (2013) 91–98.
- [7] H. Bahruji, M. Bowker, P.R. Davies, F. Pedrono, *Appl. Catal. B* 107 (2011) 205–209.
- [8] M. Hara, J. Nunoshige, T. Takata, J.N. Kondo, K. Domen, *Chem. Commun.* (2003) 3000–3001.
- [9] K. Lalitha, G. Sadanandam, V.D. Kumari, M. Subrahmanyam, B. Sreedhar, N.Y. Hebalkar, *J. Phys. Chem. C* 114 (2010) 22181–22189.
- [10] T. Sakata, T. Kawai, *Chem. Phys. Lett.* 80 (1981) 341–344.
- [11] M. Cargnello, A. Gasparotto, V. Gombac, T. Montini, D. Barreca, P. Fornasiero, *Eur. J. Inorg. Chem.* (2011) 4309–4323.
- [12] C. Minerio, A. Bedini, V. Maurino, *Appl. Catal. B* 128 (2012) 135–143.
- [13] Y. Ma, Q. Xu, X. Zong, D.G. Wang, G.P. Wu, X. Wang, C. Li, *Energy Environ. Sci.* 5 (2012) 6345–6351.
- [14] G.P. Wu, T. Chen, X. Zong, H.J. Yan, G.J. Ma, X.L. Wang, Q. Xu, D.G. Wang, Z.B. Lei, C. Li, *J. Catal.* 253 (2008) 225–227.
- [15] Q.A. Xu, Y. Ma, J. Zhang, X.L. Wang, Z.C. Feng, C. Li, *J. Catal.* 278 (2011) 329–335.
- [16] G.L. Chiarello, M.H. Aguirre, E. Selli, *J. Catal.* 273 (2010) 182–190.
- [17] K. Maeda, H. Hashiguchi, H. Masuda, R. Abe, K. Domen, *J. Phys. Chem. C* 112 (2008) 3447–3452.
- [18] K. Maeda, K. Teramura, D.L. Lu, T. Takata, N. Saito, Y. Inoue, K. Domen, *Nature* 440 (2006) 295–295.
- [19] K. Maeda, K. Teramura, K. Domen, *J. Catal.* 254 (2008) 198–204.
- [20] G.R. Bamwenda, S. Tsubota, T. Kobayashi, M. Haruta, *J. Photochem. Photobiol. A* 77 (1994) 59–67.
- [21] J.G. Yu, J.R. Ran, *Energy Environ. Sci.* 4 (2011) 1364–1371.
- [22] D.F. Ollis, E. Pelizzetti, N. Serpone, in: N. Serpone, E. Pelizzetti (Eds.), *Photocatalysis – Fundamentals and Applications*, John Wiley & Sons, New York, 1989, pp. 620–629.
- [23] D.F. Ollis, *J. Phys. Chem. B* 109 (2005) 2439–2444.
- [24] A. Mills, C. O'Rourke, K. Moore, *J. Photochem. Photobiol. A* 310 (2015) 66–105.
- [25] T. Huizinga, R. Prins, *J. Phys. Chem.* 85 (1981) 2156–2158.
- [26] P. Gajardo, T.M. Apple, C. Dybowski, *Chem. Phys. Lett.* 74 (1980) 306–308.
- [27] H. Liu, H.T. Ma, X.Z. Li, W.Z. Li, M. Wu, X.H. Bao, *Chemosphere* 50 (2003) 39–46.
- [28] K. Maeda, N. Sakamoto, T. Ikeda, H. Ohtsuka, A.K. Xiong, D.L. Lu, M. Kanehara, T. Teranishi, K. Domen, *Chem. Eur. J.* 16 (2010) 7750–7759.
- [29] B. Kraeutler, A.J. Bard, *J. Am. Chem. Soc.* 100 (1978) 5985–5992.
- [30] A. Gallo, M. Marelli, R. Psaro, V. Gombac, T. Montini, P. Fornasiero, R. Pievo, *V. Dal Santo, Green Chem.* 14 (2012) 330–333.
- [31] M. Bowker, C. Morton, J. Kennedy, H. Bahruji, J. Greves, W. Jones, P.R. Davies, C. Brookes, P.P. Wells, N. Dimitratos, *J. Catal.* 310 (2014) 10–15.
- [32] R.R. Davda, J.W. Shabaker, G.W. Huber, R.D. Cortright, J.A. Dumesic, *Appl. Catal. B* 43 (2003) 13–26.
- [33] J.W. Shabaker, R.R. Davda, G.W. Huber, R.D. Cortright, J.A. Dumesic, *J. Catal.* 215 (2003) 344–352.
- [34] H.J. Kim, S.M. Choi, S. Green, G.A. Tompsett, S.H. Lee, G.W. Huber, W.B. Kim, *Appl. Catal. B* 101 (2011) 366–375.
- [35] H. Wang, Y. Zhao, Z. Jusys, R.J. Behm, *J. Power Sources* 155 (2006) 33–46.
- [36] H. Wang, Z. Jusys, R.J. Behm, *Electrochim. Acta* 54 (2009) 6484–6498.
- [37] S. Sato, J.M. White, *J. Am. Chem. Soc.* 102 (1980) 7206–7210.
- [38] D. Panayotov, M. Mihaylov, D. Nihtianova, T. Spassov, K. Hadjiivanov, *Phys. Chem. Chem. Phys.* 16 (2014) 13136–13144.
- [39] S.K. Milonjic, *J. Serb. Chem. Soc.* 72 (2007) 1363–1367.
- [40] J.F. Montoya, M.F. Atitar, D.W. Bahnemann, J. Peral, P. Salvador, *J. Phys. Chem. C* 118 (2014) 14276–14290.
- [41] P. Chowdhury, G. Malekshoar, M.B. Ray, J. Zhu, A.K. Ray, *Ind. Eng. Chem. Res.* 52 (2013) 5023–5029.

- [42] T.A. McMurray, J.A. Byrne, P.S.M. Dunlop, J.G.M. Winkelman, B.R. Eggins, E.T. McAdams, *Appl. Catal. A* 262 (2004) 105–110.
- [43] C. Minero, G. Mariella, V. Maurino, E. Pelizzetti, *Langmuir* 16 (2000) 2632–2641.
- [44] P. Salvador, *J. Phys. Chem. C* 111 (2007) 17038–17043.
- [45] I.M. Brookes, C.A. Muryn, G. Thornton, *Phys. Rev. Lett.* 87 (2001) 226103.
- [46] R.F. Howe, M. Gratzel, *J. Phys. Chem.* 91 (1987) 3906–3909.
- [47] M.A. Henderson, *Surf. Sci. Rep.* 46 (2002) 1–308.
- [48] A. Imanishi, T. Okamura, N. Ohashi, R. Nakamura, Y. Nakato, *J. Am. Chem. Soc.* 129 (2007) 11569–11578.
- [49] B.D. McGinnis, V.D. Adams, E.J. Middlebrooks, *Chemosphere* 45 (2001) 101–108.
- [50] B.D. McGinnis, V.D. Adams, E.J. Middlebrooks, *Water Res.* 34 (2000) 2346–2354.
- [51] J.A. Dean, in: J.A. Dean (Ed.) *Lange's Handbook of Chemistry* (15th edition), McGRAW-HILL, New York, 1999, pp. 6.1–6.50.
- [52] B. Sklarz, *Q. Rev. Chem. Soc.* 21 (1967) 3–28.
- [53] M. Minella, M.G. Faga, V. Maurino, C. Minero, E. Pelizzetti, S. Coluccia, G. Martra, *Langmuir* 26 (2010) 2521–2527.
- [54] I.A. Shkrob, M.C. Sauer, D. Gosztola, *J. Phys. Chem. B* 108 (2004) 12512–12517.
- [55] K.U. Ingold, in: J.K. Kochi (Ed.), *Free Radicals*, vol. 1, John Wiley & Sons, New York, 1973, pp. 37–112.
- [56] X.D. Gu, W.J. Zhang, R.G. Salomon, *J. Org. Chem.* 77 (2012) 1554–1559.
- [57] J.J. Orlando, G.S. Tyndall, T.J. Wallington, *Chem. Rev.* 103 (2003) 4657–4689.
- [58] O.I. Micic, Y.N. Zhang, K.R. Cromack, A.D. Trifunac, M.C. Thurnauer, *J. Phys. Chem.* 97 (1993) 13284–13288.
- [59] J. Schneider, D.W. Bahnemann, *J. Phys. Chem. Lett.* 4 (2013) 3479–3483.
- [60] H. Harada, T. Ueda, T. Sakata, *J. Phys. Chem.* 93 (1989) 1542–1548.
- [61] N. Hykaway, W.M. Sears, H. Morisaki, S.R. Morrison, *J. Phys. Chem.* 90 (1986) 6663–6667.
- [62] I.A. Shkrob, J.K.S. Wan, *Res. Chem. Intermediat.* 18 (1992) 19–47.
- [63] H. Wang, Z. Jusys, R.J. Behm, *J. Electroanal. Chem.* 595 (2006) 23–36.
- [64] G.P. Wu, T. Chen, W.G. Su, G.H. Zhou, X. Zong, Z.B. Lei, C. Li, *Int. J. Hydrogen Energy* 33 (2008) 1243–1251.
- [65] H. Hashiguchi, K. Maeda, R. Abe, A. Ishikawa, J. Kubota, K. Domen, *Bull. Chem. Soc. Jpn.* 82 (2009) 401–407.
- [66] H.A. Schwarz, R.W. Dodson, *J. Phys. Chem.* 88 (1984) 3643–3647.